Dynamic RF Beam Steering Using Photo-Induced Fresnel Zone Plates on Solar Cells

Dynamic RF Beam Steering Using Photo-Induced Fresnel Zone Plates on Solar Cells

Zahra Sepehri, *Graduate Student Member, IEEE,* Gianluca Fabi, *Member, IEEE,* Marco Farina, *Senior Member, IEEE,* and Richard Al Hadi, *Senior Member, IEEE*

***Abstract*—Optically reconfigurable beam steering at millimeter-wave (mm-wave) frequencies requires engineered semiconductor surfaces with high-power optical sources. This paper presents the first demonstration of beam steering using a commercially available monocrystalline silicon solar cell, directly exploiting its intrinsic photovoltaic properties for electromagnetic wave modulation. Dynamically reconfigurable Fresnel Zone Plate (FZP) patterns are projected onto the solar cell with low-power visible light (0.043 W/cm^2), enabling reconfigurable beam steering across the Ka-band (26.4-40 GHz). The solar cell's back-contact design preserves RF transparency while providing polarization isolation up to -25 dB, and measurements show 10 dB modulation depth under illumination. Simulations and experiments confirm diffraction-based steering of a 30-GHz source. Furthermore, a 5G New Radio (NR) data-link experiment at 28.03 GHz using 256-QAM modulation demonstrates the system's capability to sustain high-rate communication links. This fabrication-free and accessible approach establishes a practical path toward reconfigurable mm-wave beam steering and adaptive RF devices.**

***Index Terms*—Millimeter-wave, dynamic beam-steering, Fresnel Zone Plates, FZP, semiconductor photo modulation, optoelectronic, communication, 5G.**

I. Introduction

MILLIMETER-WAVE frequencies play a crucial role in 5G networks by addressing spectrum congestion and supporting the growing demand for high data rates [1], [2]. However, their short wavelengths result in propagation losses, multi-path delay, and atmospheric attenuation [3]. To mitigate these limitations, beam steering techniques are employed to enhance the performance of communication channels by directing radiated power toward intended receivers, thereby extending coverage [4].

Traditional reconfigurable beam steering solutions, such as phased array antennas [5], [6], reconfigurable transmitarray [7], quasi-optical systems [8]–[11], leaky-wave antennas [12], and metamaterials/metasurfaces [13], are often limited by high cost, power consumption, complex architectures, and challenging implementation requirements [3], [14].

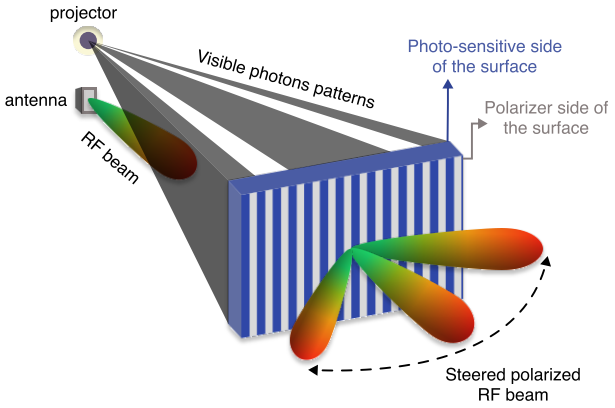

Fig. 1. Working principle of the implemented design: the surface steers the RF beam by photo-projection.

One promising yet simple and cost-effective approach for beam steering is the use of reconfigurable FZPs. It enables dynamic control of beam direction through spatial modulation of electromagnetic waves. This is demonstrated through the use of mechanically rotating metal shutters, which create reconfigurable transparent and opaque zones to focus the beam at a desired angle [15]. The use of FZPs for RF diffraction has also been explored in previous works [16]–[18]. RF spatial modulation can also be achieved by photo-exciting a semiconductor to locally modulate charge carrier density [19]–[24]. Whenever a semiconductor (like silicon or germanium) is exposed to light with a photon energy above its band gap, free carriers are generated. This variation in charge carrier density alters the refractive index of the photo-excited semiconductor, enabling controlled attenuation/reflection of electromagnetic waves [25]. As a result, the generated FZPs diffract the incident wave, producing a steerable beam [26], [27]. However, achieving sufficient attenuation of mm-waves by photo-exciting a semiconductor is challenging, as it requires high optical illumination densities [19]. Early demonstrations employed near infrared (NIR) radiation [26] or pulsed lasers with power densities reaching up to 100 W/cm^2 [28] to modulate the semiconductor surface. Previous approaches have explored the use of prisms [21], plasmonic resonances [29], meta-surfaces [30], and planar cavities [31] to enhance light–semiconductor interactions. Other implementations have used visible-light projectors with power densities in the or-

Received September 22, 2025; revised October 31, 2025; accepted November XX, 2025. This work was supported in part by the Natural Sciences and Engineering Research Council of Canada (NSERC) under Grant RGPIN-2025-05459. *(Corresponding author: Richard Al Hadi)*

Zahra Sepehri and Richard Al Hadi are with Electrical Engineering Department, École de technologie supérieure, Université du Québec, Montreal, QC, H3C 1K3, Canada (e-mail: alhadi@ieee.org).

Gianluca Fabi is with Institute of Biophysics, Johannes Kepler University, 4040 Linz, Austria.

Marco Farina is with Information Engineering Department, Polytechnic University of Marche, 60131 Ancona, Italy.

Digital Object Identifier XX.XXX/TMTT.2025.XXXXXXX

TABLE I
COMPARISON OF PHOTO-EXCITING SEMICONDUCTORS USED FOR BEAM STEERING VIA SORET FZPS.

Publication	Frequency (GHz)	Optical source	Irradiance (W/cm^2)	Surface material	Area (cm^2)	Steering Angle (°)	Efficiency (%)	Data link
[26]	94	Near-infrared LED	0.4–8.17[a]	Silicon wafer	177	±30	10[b]	–
[28]	35	Pulsed laser	100	Silicon wafer	314	±20	6–14[b]	–
[14], [19]	94	Visible light	0.07	Passivated Silicon	78.5	±45	4.8–6[c]	–
[35]	740	Visible light	2	Passivated Silicon	3.2	±8	7.1[c]	–
This work	30	Visible light	0.043	Solar cell	88.8	±27	4–5.5[d]	5G NR, 256-QAM 0.4 GHz, 3.9 Gbps EVM <4.5%

[a] Estimated range based on available components. [b] Theoretical efficiency limit. [c] Excluding semiconductor-induced losses. [d] Measured efficiency including semiconductor-induced losses.

der of 70 mW/cm^2 to generate these patterns, significantly reducing both cost and system complexity [19]. However, the improvement is made possible by specialized surface engineering.

Bare semiconductors suffer from a high recombination rate of photo-excited carriers at the surface, preventing the accumulation of free carriers necessary for effective modulation. To address this issue and enhance photo-modulation without increasing the illumination intensity, surface passivation techniques are needed [19], [22], [32]. These techniques reduce the density of surface states and surface concentration of electrons or holes. Surface passivation methods for crystalline silicon include dielectric film deposition, chemical surface treatments, and the formation of p-n junctions or heterojunctions using materials like amorphous silicon [33]. More recently, the deposition of Al_2O_3 [34] or silicon-on-sapphire [22] has been shown to passivate silicon wafers, enhancing mm-wave modulation by significantly reducing carrier recombination. This process reduces carrier recombination, resulting in longer carrier lifetime and higher photoconductivity. Surface passivation is a complex process that requires careful control of material quality, surface preparation, and deposition techniques [34].

In this paper, we demonstrate a novel approach for mm-wave beam steering based on a commercially available monocrystalline silicon solar cell as illustrated in Fig. 1. To the best of our knowledge, this is the first demonstration of directly exploiting a solar cell's intrinsic photovoltaic properties to modulate electromagnetic waves. The main contributions of this work are as follows. First, we show that photo-induced FZP patterns projected onto the solar cell enable non-mechanical beam steering at Ka-band, validated through both full-wave simulations and experimental measurements. Second, the approach achieves effective modulation under low-power visible illumination (0.043 W/cm²), whereas prior demonstrations relied on high-power optical sources or surface-passivated wafers (Table I). Third, the method is fabrication-free and based entirely on off-the-shelf components, establishing a practical and reproducible platform for optically reconfigurable RF systems. These features distinguish the present work from conventional optically controlled beam-steering techniques.

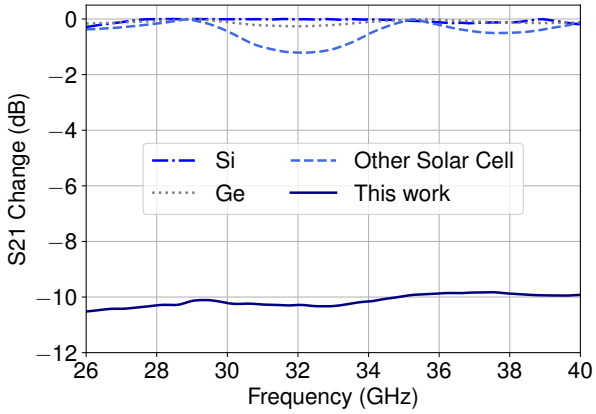

Fig. 2. Measured relative change in S21 of tested surfaces under optical illumination, using the non-illuminated condition as the reference baseline.

II. PHOTO-EXCITED SURFACE FOR RF MODULATION

A key factor in efficient photo-induced beam steering is the selection of a surface with strong mm-wave attenuation (6–10 dB) under optical illumination. Strong attenuation in photo-induced FZP Antennas is essential for inducing metallic-like electromagnetic behavior within the illuminated regions. Additionally, increasing the contrast between transmissive and blocking zones enhances constructive and destructive interference, resulting in more effective spatial modulation, improved beam directivity, and overall system performance [14]. The photo-induced attenuation exhibited by the surface is primarily determined by the density of excess free carriers generated under optical illumination. The carrier density depends on several parameters, including the incident optical power density, the illumination wavelength relative to the material's bandgap, the carrier lifetime, and the surface recombination velocity. In addition to free-carrier effects, the physical thickness of the substrate influences how the incident electromagnetic wave interacts with the surface. In particular, how it affects the relative proportions of the wave that are transmitted and reflected [19].

While several semiconductor materials could, in principle, support photo-induced mm-wave modulation, their practical effectiveness depends on achieving significant attenuation when illuminated by a low-power optical source. To identify

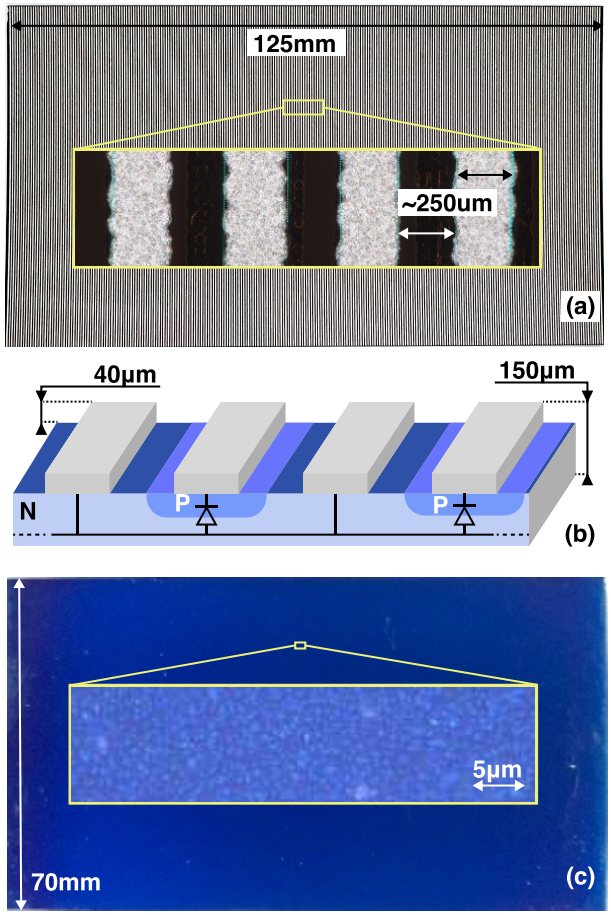

Fig. 3. (a) Macro- and micro-scale view of the electrical side of the surface. (b) Simplified 3D schematic representation of the solar cell. (c) Macro- and micro-scale view of the photo-sensitive side of the surface.

a suitable candidate, we compared high-resistivity silicon (10k Ohm.cm), germanium, and available solar cells. The results, shown in Fig. 2, indicate that untreated semiconductors produce negligible modulation, with the forward transmission coefficient (S21) changing by only 0.1 dB across 26-40 GHz.

In contrast to untreated semiconductors, the monocrystalline silicon solar cell used in this study achieves approximately 10 dB of attenuation under optical illumination. Other tested solar cells have front and back metalization layers that prevent the RF wave from propagating through the surface. As a result, they are reflective to electromagnetic waves under both illuminated and non-illuminated conditions.

The solar cell used in this work, is a commercially available monocrystalline silicon panel from SunPower's Maxeon cells, [36] featuring a fully exposed photo-sensitive side (Fig. 3(c)) and an electrical side patterned with a tin-coated copper metal grid (Figures 3(a) and (b)). The underlying structure consists of an N-type substrate with P-type doped regions, forming multiple p-n junctions. When the solar cell is illuminated, photons with energies above the semiconductor band gap excite electrons from the valence band to the conduction band, generating electron–hole pairs. The built-in electric field across the p–n junction separates the carriers, driving electrons toward the

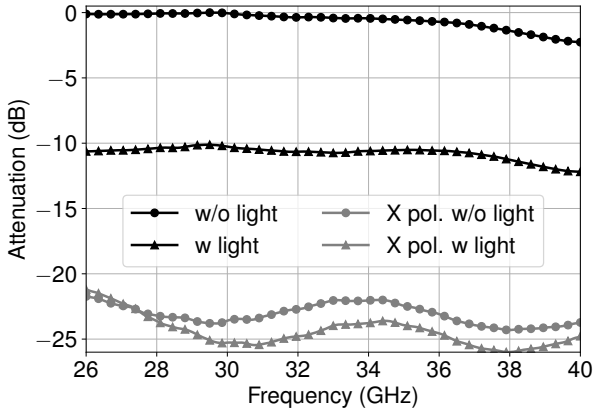

Fig. 4. Measured effect of surface projection on transmission for E-polarization and cross-polarization orientations (X pol.).

n-type region and holes toward the p-type region. This reduces recombination, increases the free carrier density, and enhances the local conductivity of the semiconductor [37]. In addition, the cell's passivation layer further reduces recombination at surface defects, such as dangling bonds, increasing both the carrier lifetime and the density of photo-generated carriers under illumination. These intrinsic features make the solar cell inherently capable of modulating electromagnetic waves. The solar cell consists of a silicon layer with a relative permittivity of $\varepsilon_r \approx 11.7$, consistent with standard values for undoped Si at mm-wave frequencies. The substrate is significantly thinner than the thickness required for Fabry-Pérot resonance, so no substantial standing wave effects are expected within the slab. The material is non-magnetic, with relative permeability as $\mu_r \approx 1$. The copper grid lines on the electrical side act as a polarization-selective layer. Depending on its orientation relative to the polarization of the incoming electromagnetic wave, the parallel conductive lines either allow transmission or, in the case of cross-polarization, provide isolation of up to -25 dB. The effect of surface projection on transmission for both E-polarization and cross-polarization orientations is illustrated in Fig. 4. To optimize the solar cell as a photo-induced surface, the only modification made is the removal of grid-line interconnections. This adjustment confines free carrier movement and prevents their distribution across the surface via metallic grid lines while reducing the substrate area to 70×125 mm^2. These properties make the solar cell a suitable surface for implementing reconfigurable FZPs.

The effect of illumination intensity on RF modulation is shown in Fig. 5. The normalized transmission coefficient (S21) at 30 GHz decreases with increasing optical power, confirming that higher light intensity generates more photo-induced carriers and enhances attenuation.

The FZP pattern used in this work consists of alternating transparent and opaque stripes, categorized as a Soret Zone Plate. While the Soret Zone Plate has the lowest efficiency among FZP types, it offers advantages in simplicity and low cost [19]. It is used to focus mm-waves by manipulating wave propagation through these alternating regions, where the opaque stripes ideally reflect the wave, while the transparent

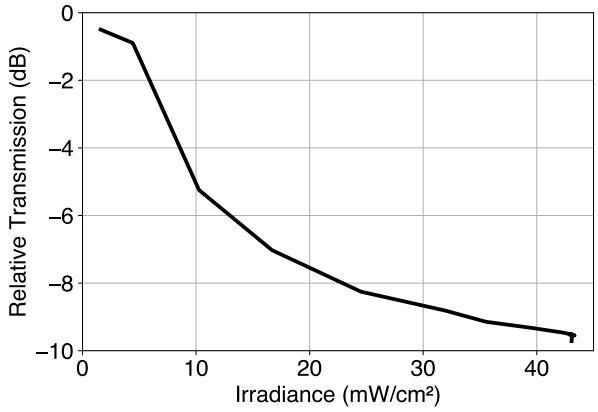

Fig. 5. Normalized measured S21 parameter at 30 GHz as a function of power density of the projected light.

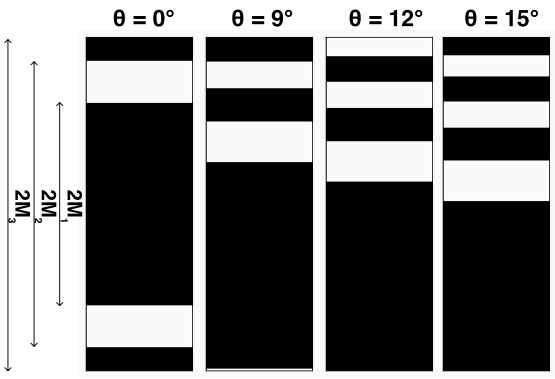

Fig. 6. FZP patterns designed for a focal length of $F = 140\,\text{mm}$, aperture size of $D = 125\,\text{mm}$, and an operating frequency of 30 GHz. The white regions represent the illuminated areas.

zones allow transmission. Opacity is achieved by exposing the surface to light, whereas transparency results from the absence of light. The positions of these zones are determined based on the desired steering angle, operating frequency, and the focal point of the antenna feed [15]. In this work, the optical patterns projected onto the semiconductor surface are computationally optimized using the Fresnel zone equations to achieve optimal beam focusing and steering performance. In this design, the feed antenna is located at the focal point of the FZP $(x = 0, z = -F)$. Under these conditions, the phase across the surface is given by $\psi(x) = k\left(\sqrt{x^2 + F^2} - F\right)$, where $k = (2\pi)/\lambda$ and λ is the wavelength. For a beam steered with an angle θ_0, the desired phase is $\psi_d = kx\sin\theta_0$. The FZP generates a phase difference of $\psi_L = \psi_d - \psi(x)$, with the maximum phase position $x_c = F\tan\theta_0$. Contours of constant phase are determined by

$$\psi_L = \psi_d - \psi(x) = \psi_{\max} - n\pi, \quad n = 0, 1, 2, \ldots \tag{1}$$

where $\psi_{\max} = \psi_L(x_c)$. The center x_{cn} and half-length M_n of the same zone can be calculated using the following equations:

$$x_{cn} = \frac{a_n \sin\theta_0}{\cos^2\theta_0}, \tag{2}$$

TABLE II
VALUES OF x_{cn} AND M_n AT 30 GHZ, $F = 140$ MM.
ALL UNITS ARE IN MM.

θ_0	0°		9°		12°		15°	
n	x_{cn}	M_n	x_{cn}	M_n	x_{cn}	M_n	x_{cn}	M_n
1	0	37.74	22.97	38.46	30.84	39.02	38.89	39.77
2	0	53.85	23.77	54.87	31.93	55.68	40.28	56.76
3	0	66.52	24.57	67.78	33.01	68.80	41.67	70.13
4	0	77.45	25.38	78.94	34.10	80.12	43.06	81.69
5	0	87.32	26.18	89.00	35.19	90.34	44.44	92.11
6	0	96.43	26.98	98.30	36.27	99.79	45.83	101.75
7	0	105.00	27.78	107.04	37.36	108.67	47.22	110.82

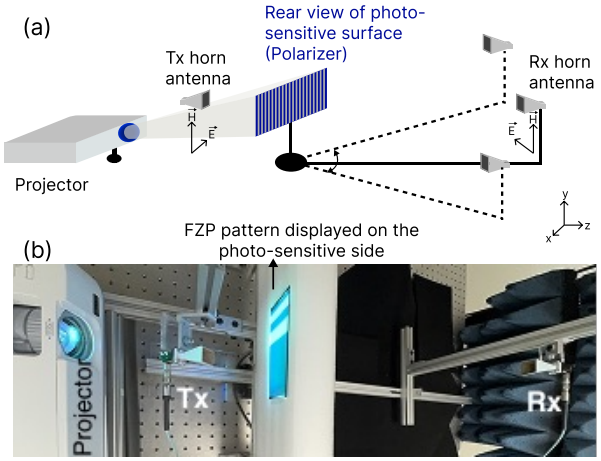

Fig. 7. (a) Measurement setup illustration, (b) photograph of the setup. The FZP patterns are projected onto the photo-sensitive surface, and the receiver mechanically scans the area. The E-plane of the antenna and the surface are aligned parallel for consistent polarization orientation.

$$M_n = \frac{\sqrt{a_n^2 - F^2 + x_{cn}^2\cos^2\theta_0}}{\cos\theta_0}, \tag{3}$$

where [15]

$$a_n = F - \frac{\psi_{\max} - n\pi}{k}. \tag{4}$$

Using these equations, the positions of the zone centers (x_{cn}) and their widths $(2M_n)$ are determined. Table II presents these values for steering angles 0°, 9°, 12°, and 15°, (symmetrical to -9°, -12°, and -15°) at the wavelength of 10 mm, with a focal length F = 140 mm. Fig. 6 illustrates the corresponding patterns based on the values presented in Table II, considering the surface dimensions.

III. RESULTS AND DISCUSSION

The beam-steering setup is illustrated in Fig. 7. A commercial 3000-lumen projector illuminates the photo-sensitive side of the solar cell with an optical power density of 43 mW/cm². Two 15 dBi horn antennas connected to a Vector Network Analyzer (VNA) operating at the 26.4-40 GHz range. The transmitter is positioned at the theoretical focal length of the designed FZP patterns, while the receiving antenna is located in the calculated far-field of the transmitter. The solar cell surface is oriented with its polarizer lines perpendicular to

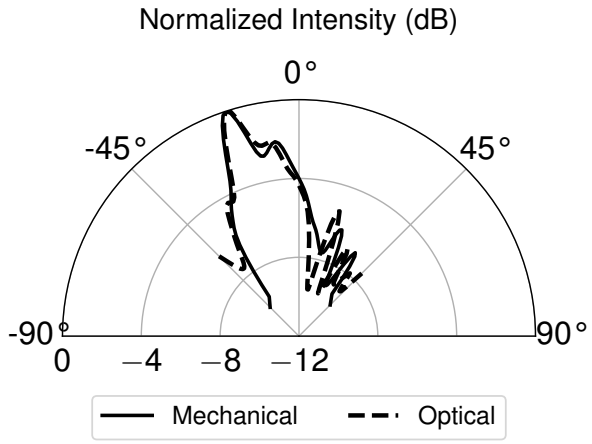

Fig. 8. Comparison of radiation patterns measured by mechanical scanning (Rx rotated over all angles) and optical scanning (Rx fixed at –18°, with projected FZP patterns corresponding to different scan angles).

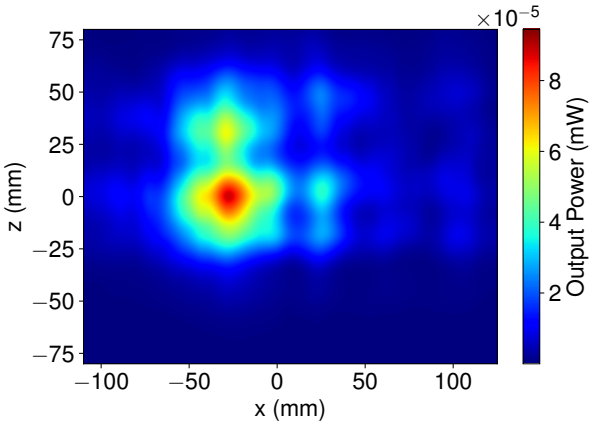

Fig. 9. 2D plot of the received power with an input power of –5 dBm, using the FZP pattern designed for –12° beam steering. The peak is observed at approximately –42.5 mm, consistent with the expected beam position.

the E-plane to maximize transmission. Beam-steering at -18° is validated using two methods: mechanical rotation of the receiver and optical scanning via sequential FZP projection. Both methods yield closely matching radiation patterns at 30 GHz in Fig. 8, confirming that optical scanning reliably characterizes the steered beam without mechanical motion. A 2D spatial scan at 30 GHz for the FZP steering to -12° shows the main lobe aligned with the expected E-plane direction in Fig. 9, demonstrating effective beam steering. Minor asymmetry along the z-axis likely arises from illumination non-uniformity or slight misalignments of the setup. Despite the binary FZP design and low optical power, the measured main lobe confirms that this approach provides a practical, low-cost alternative to more complex metasurface or high-power implementations.

To further validate the experimental results, full-wave simulations of the beam-steering system are performed. In the model (Fig. 10), illuminated regions act as perfect conductors and unilluminated regions act as unexcited silicon. This allows the simulation to approximate how FZP patterns affect RF

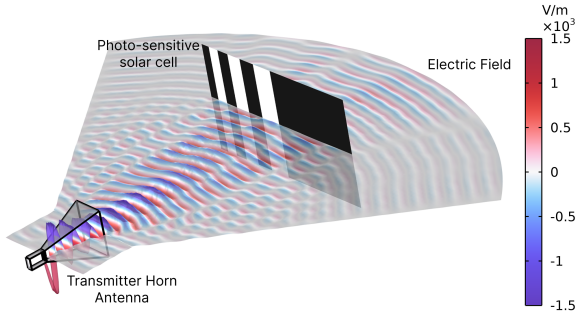

Fig. 10. Simulation model of the photo-sensitive side of the solar cell with projected FZP patterns. White zones indicate illuminated regions, while black zones correspond to non-illuminated areas.

TABLE III
MEASURED AND SIMULATED ANTENNA PERFORMANCE AT 30 GHZ.

Steering angle	Gain (dBi)		Efficiency (%)	
	Meas	Sim	Meas	Sim
±9°	11	12	5.5	6
±12°	11	11	4	6
±15°	10	11	4	5

propagation. As seen in Figs. 11(a)–(f), the simulated and measured patterns at 30 GHz agree well for all steering angles, confirming that the system reliably achieves the intended beam directions.

IV. Performance Evaluation and Application

Measured S11 and VSWR for three representative FZP patterns (±9°, ±12°, ±15°) across 26–40 GHz, shown in Fig. 12, remain below –20 dB and 1.2, respectively, indicating consistently low reflection across the steering range. Simulated S11 values at 30 GHz closely match measurements (–17.4 dB to –20.1 dB), validating the simulation model.

The focal length-to-aperture ratio (F/D = 1.12, with focal length 140 mm and aperture diameter 125 mm) represents a compromise between aperture efficiency and practical constraints. This yields a taper efficiency of 60% and full spillover efficiency; however, the overall system efficiency remains below 10% due to diffraction loss from the binary-blocking FZP, a known limitation of Soret-type designs. Table III reports the measured and simulated antenna efficiency at 30 GHz, showing good agreement with the simulation. The measured radiation patterns exhibit elevated sidelobes (typically in the range of -2 to -4 dB) under beam-steering conditions. These higher sidelobe levels are primarily attributed to the distortion of the ideal Gaussian profile caused by the presence of the surface, the F/D ratio of the proposed design [35], and the inherent limitations of the binary-blocking FZP structure. While this represents a known limitation of the current approach, future work will focus on optimizing key parameters to enhance sidelobe suppression and improve overall beam quality.

To validate data-link performance, we established a 5G NR FR2 (n261) communication channel at 28.03 GHz using a 256-QAM modulation scheme and steered the beam direction with

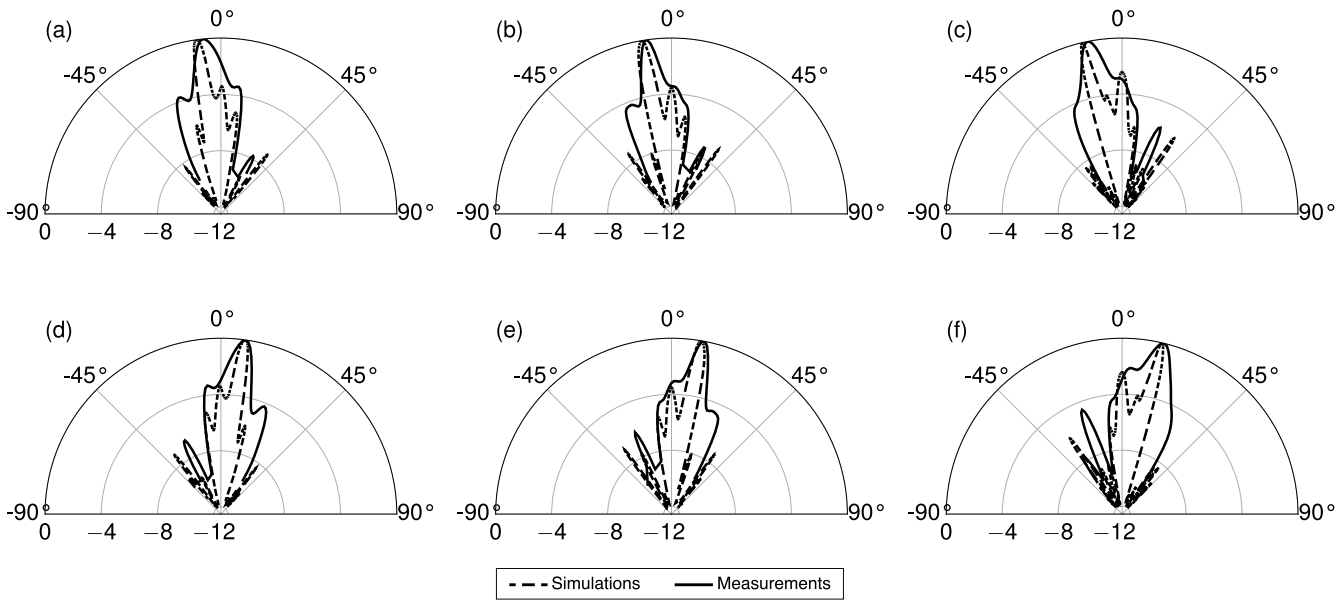

Fig. 11. Simulated and measured polar representation of normalized beam patterns at different steering angles in dB: (a) -9°, (b) -12°, (c) -15°, (d) +9°, (e) +12°, and (f) +15°.

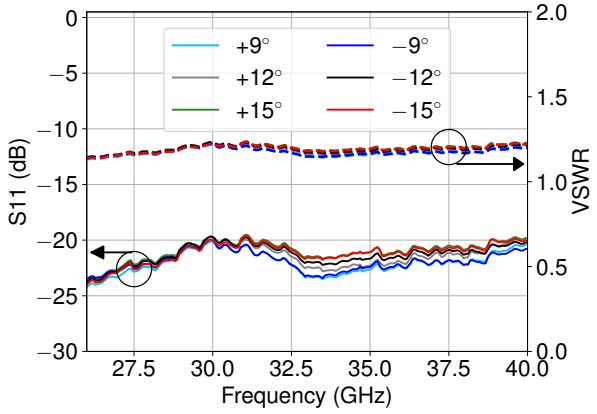

Fig. 12. Measured S11 a for FZP patterns designed for ±9°, ±12°, and ±15° beam steering angles.

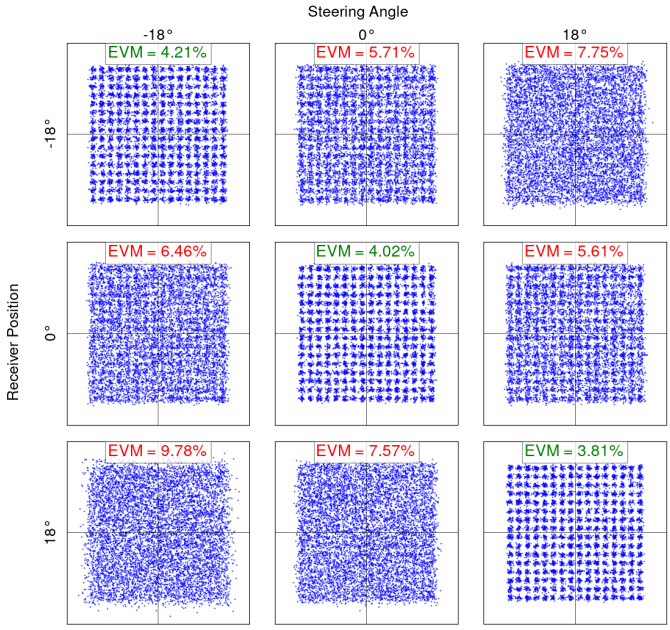

Fig. 13. Measured constellations and EVMs for different steering angles and receiver positions using 256-QAM modulation scheme, 400 MHz bandwidth and data rate of 3.932 Gbps.

the computationally optimized visible-light mask to 0°, +18°, and -18°. A standard NR waveform is generated at 28.03 GHz with a vector signal generator; the received signal produces constellation plots and RMS Error Vector Magnitude (EVM) (3GPP-style [38]) at each steering angle. When the steering angle and the receiver position are aligned, the 256-QAM constellations remain tightly clustered with low EVM, indicating that the surface introduces no format-specific distortion and that link quality is dominated by SNR. As the receiver moves off the steered look-angle, the constellations exhibit symbol spreading and the EVM increases in accordance with the expected pointing-loss penalty. Fig. 13 presents the measured EVM values and corresponding constellation diagrams for the evaluated steering scenarios. These results confirm the proposed optically reconfigurable aperture reliably supports NR-class data links within the Ka-band, maintaining EVM below the 256-QAM (4.5% [39]) specification limit when the steering direction and receiver are aligned.

V. Conclusion

This work presents a reconfigurable and low-cost mono-crystalline silicon solar cell for scalable and dynamic mm-wave beam steering. Low-power visible illumination induces

modulation, while spatial FZP patterns control beam direction across the Ka-band. The experimental validation of 5G NR data link using 256-QAM modulation confirms that the proposed aperture sustains high-capacity communication with EVM below standard limits. These results confirm that the photo-excited solar cell enables optical beam control while preserving signal integrity, establishing it as a previously unexplored candidate for accessible reconfigurable RF systems and for advancing light-controlled modulation research in imaging, adaptive antennas, and other mm-wave and terahertz applications.

ACKNOWLEDGMENTS

The authors would like to thank Dr. Mathieu Gratuze, Prof. Antonio Morini, Mr. Amin Pourvali, and Mr. Meysam Naghizadeh for all their support.

REFERENCES

[1] W. Hong, Z. H. Jiang, C. Yu, D. Hou, H. Wang, C. Guo, Y. Hu, L. Kuai, Y. Yu, Z. Jiang, Z. Chen, J. Chen, Z. Yu, J. Zhai, N. Zhang, L. Tian, F. Wu, G. Yang, Z.-C. Hao, and J. Y. Zhou, "The role of millimeter-wave technologies in 5G/6G wireless communications," *IEEE Journal of Microwaves*, vol. 1, no. 1, pp. 101–122, 2021.

[2] Y. Niu, Y. Li, D. Jin, L. Su, and A. V. Vasilakos, "A survey of millimeter wave communications (mmwave) for 5G: opportunities and challenges," *Wireless networks*, vol. 21, pp. 2657–2676, 2015.

[3] A. Bansal, C. J. Panagamuwa, and W. G. Whittow, "State-of-the-art millimeter-wave beam steering antennas for beyond 5G and 6G networks: A comprehensive review," *Antennas and Propagation Magazine*, vol. 66, no. 5, pp. 40–51, 2024.

[4] J. Kibiłda, A. B. MacKenzie, M. J. Abdel-Rahman, S. K. Yoo, L. G. Giordano, S. L. Cotton, N. Marchetti, W. Saad, W. G. Scanlon, A. Garcia-Rodriguez, D. López-Pérez, H. Claussen, and L. A. DaSilva, "Indoor millimeter-wave systems: Design and performance evaluation," *Proceedings of the IEEE*, vol. 108, no. 6, pp. 923–944, 2020.

[5] N. Li, Z. Ma, X. Xie, Y. Yuan, B. Lan, H. Lu, H. Gao, S. Wang, C. Song, Q. Jane Gu, and Z. Xu, "A Ka-band 64-element four-beam phased array receiver with inter-beam interference cancellation," *IEEE Transactions on Microwave Theory and Techniques*, vol. 73, no. 1, pp. 221–233, 2025.

[6] X. Zhi, K. Huang, Q. Zhang, B. Zhang, Z. Zhu, and L. Ran, "A self-adaptive phased array conformed on a highly flexible aperture," *IEEE Transactions on Microwave Theory and Techniques*, vol. 73, no. 3, pp. 1821–1836, 2025.

[7] R. Cane, R. Sauleau, and M. Alouini, "Optically-controlled unit-cell for transmitarrays at x-band," in *2019 49th European Microwave Conference (EuMC)*. IEEE, 2019, pp. 714–717.

[8] A. Azari, A. Skrivervik, and H. Aliakbarian, "Design of a novel wide-angle rotman lens beamformer for 5G mmwave applications," *Scientific Reports*, vol. 14, no. 1, p. 1245, 2024.

[9] S. K. Karki, M. Varonen, M. Kaunisto, A. Rantala, M. Lahti, A. Lamminen, J. Holmberg, M. Kantanen, J. Ala-Laurinaho, and V. Viikari, "Beam-reconfigurable antenna based on vector modulator and rotman lens on ltcc," *IEEE access*, vol. 9, pp. 52 872–52 882, 2021.

[10] J. G. Marin and J. Hesselbarth, "Lens antenna with planar focal surface for wide-angle beam-steering application," *IEEE Transactions on Antennas and Propagation*, vol. 67, no. 4, pp. 2757–2762, 2019.

[11] Y. Shi, Y. Deng, P. Li, P. Fay, and L. Liu, "A 200 GHz fully integrated, polarization-resolved quasi-optical detector using zero-bias heterostructure backward diodes," *IEEE Microwave and Wireless Components Letters*, vol. 32, no. 7, pp. 891–894, 2022.

[12] K. W. Eccleston, "Mode analysis of the corrugated substrate integrated waveguide," *IEEE Transactions on Microwave Theory and Techniques*, vol. 60, no. 10, pp. 3004–3012, 2012.

[13] H. Li, C. Ma, F. Shen, K. Xu, D. Ye, J. Huangfu, C. Li, L. Ran, and T. A. Denidni, "Wide-angle beam steering based on an active conformal metasurface lens," *IEEE Access*, vol. 7, pp. 185 264–185 272, 2019.

[14] T. F. Gallacher, D. A. Robertson, and G. M. Smith, "The photo-injected fresnel zone plate antenna: Optoelectronic beam steering at mm-wave frequencies," *Transactions on antennas and propagation*, vol. 61, no. 4, pp. 1688–1696, 2012.

[15] A. Petosa, S. Thirakoune, and A. Ittipiboon, "Reconfigurable fresnel-zone-plate-shutter antenna with beam-steering capability," *IEEE Antennas and Propagation Magazine*, vol. 49, no. 5, pp. 42–51, 2007.

[16] H. Li, C. Ma, D. Ye, Y. Sun, W. Zhu, C. Li, and L. Ran, "Dual-band fresnel zone plate antenna with independently steerable beams," *IEEE Transactions on Antennas and Propagation*, vol. 66, no. 4, pp. 2113–2118, 2018.

[17] Q. Xi, C. Ma, H. Li, B. Zhang, C. Li, and L. Ran, "A reconfigurable planar fresnel lens for millimeter-wave 5G frontends," *IEEE Transactions on Microwave Theory and Techniques*, vol. 68, no. 11, pp. 4579–4588, 2020.

[18] H. Li, D. Ye, F. Shen, B. Zhang, Y. Sun, W. Zhu, C. Li, and L. Ran, "Reconfigurable diffractive antenna based on switchable electrically induced transparency," *IEEE Transactions on Microwave Theory and Techniques*, vol. 63, no. 3, pp. 925–936, 2015.

[19] T. F. Gallacher, R. Sondena, D. A. Robertson, and G. M. Smith, "Optical modulation of millimeter-wave beams using a semiconductor substrate," *Transactions on Microwave Theory and Techniques*, vol. 60, no. 7, pp. 2301–2309, 2012.

[20] A. Kannegulla, M. I. B. Shams, L. Liu, and L.-J. Cheng, "Photo-induced spatial modulation of THz waves: opportunities and limitations," *Optics express*, vol. 23, no. 25, pp. 32 098–32 112, 2015.

[21] X. Liu, E. P. Parrott, B. S.-Y. Ung, and E. Pickwell-MacPherson, "Exploiting total internal reflection geometry for efficient optical modulation of terahertz light," *APL Photonics*, vol. 1, no. 7, 2016.

[22] P. Li, W. Wu, Y. Shi, Y. Deng, K. Dave, P. Fay, and L. Liu, "Integrated broadband thz switching using photoconductivity modulation in si-on-sapphire substrates," *IEEE Transactions on Terahertz Science and Technology*, 2025.

[23] Y. Deng, Y. Shi, P. Li, P. Fay, L.-J. Cheng, and L. Liu, "A cost-effective approach for achieving subwavelength THz imaging using photoinduced coded-apertures on mesa-array structures," *IEEE Transactions on Terahertz Science and Technology*, vol. 12, no. 6, pp. 658–666, 2022.

[24] S. Augustin, S. Frohmann, P. Jung, and H.-W. Hübers, "Mask responses for single-pixel terahertz imaging," *Scientific reports*, vol. 8, no. 1, p. 4886, 2018.

[25] Z. Jiang, M. I. B. Shams, L.-J. Cheng, P. Fay, J. L. Hesler, C.-y. E. Tong, and L. Liu, "Investigation and demonstration of a WR-4.3 optically controlled waveguide attenuator," *IEEE Transactions on Terahertz Science and Technology*, vol. 7, no. 1, pp. 20–26, 2016.

[26] G. Webb, W. Vernon, M. Sanchez, S. Rose, and S. Angello, "Optically controlled millimeter wave antenna," in *International Topical Meeting on Microwave Photonics*. IEEE, 1999, pp. 275–278 vol.1.

[27] J. M. Monkevich and G. P. Le Sage, "Design and fabrication of a custom-dielectric fresnel multi-zone plate lens antenna using additive manufacturing techniques," *IEEE Access*, vol. 7, pp. 61 452–61 460, 2019.

[28] M. Hajian, G. De Vree, and L. Ligthart, "Electromagnetic analysis of beam-scanning antenna at millimeter-wave band based on photoconductivity using fresnel-zone-plate technique," *Antennas and propagation magazine*, vol. 45, no. 5, pp. 13–25, 2003.

[29] T. Wen, J. Tong, D. Zhang, Y. Zhu, Q. Wen, Y. Li, H. Zhang, Y. Jing, and Z. Zhong, "Semiconductor terahertz spatial modulators with high modulation depth and resolution for imaging applications," *Journal of Physics D: Applied Physics*, vol. 52, no. 25, p. 255303, 2019.

[30] M. Kafesaki, N. Shen, S. Tzortzakis, and C. Soukoulis, "Optically switchable and tunable terahertz metamaterials through photoconductivity," *Journal of Optics*, vol. 14, no. 11, p. 114008, 2012.

[31] N. Born, M. Scheller, M. Koch, and J. V. Moloney, "Cavity enhanced terahertz modulation," *Applied Physics Letters*, vol. 104, no. 10, 2014.

[32] P. Li, W. Wu, Y. Shi, Y. Deng, P. Fay, and L. Liu, "Broadband thz switching with extremely low insertion loss and superior isolation," in *International Microwave Symposium-IMS*. IEEE, 2023, pp. 688–691.

[33] A. G. Aberle, "Surface passivation of crystalline silicon solar cells: a review," *Progress in Photovoltaics: Research and Applications*, vol. 8, no. 5, pp. 473–487, 2000.

[34] I. Hooper, N. Grant, L. Barr, S. Hornett, J. D. Murphy, and E. Hendry, "High efficiency photomodulators for millimeter wave and THz radiation," *Scientific Reports*, vol. 9, no. 1, p. 18304, 2019.

[35] M. I. B. Shams, Z. Jiang, S. M. Rahman, L.-J. Cheng, J. L. Hesler, P. Fay, and L. Liu, "A 740 GHz dynamic two-dimensional beam-steering and forming antenna based on photo-induced reconfigurable fresnel zone plates," *Transactions on Terahertz Science and Technology*, vol. 7, no. 3, pp. 310–319, 2017.

[36] D. D. Smith, P. J. Cousins, A. Masad, A. Waldhauer, S. Westerberg, M. Johnson, X. Tu, T. Dennis, G. Harley, G. Solomon *et al.*, "Generation iii high efficiency lower cost technology: Transition to full scale

manufacturing," in *2012 38th IEEE Photovoltaic Specialists Conference*. IEEE, 2012, pp. 001 594–001 597.
[37] N. Guerra, M. Guevara, C. Palacios, and F. Crupi, "Operation and physics of photovoltaic solar cells: an overview," *I+ D Tecnológico*, vol. 14, no. 2, pp. 84–95, 2018.
[38] 3GPP/ETSI, "TS 138 101-3 V17.12.0 (Release 17) – UE radio transmission and reception; Part 3: Range 3 Standalone," ETSI, Technical Specification, Feb. 2024.
[39] 3GPP/ETSI, "TS 38.141-1: NR; Base Station (BS) antenna performance – Part 1: Pattern synthesis and characterization," 3GPP, Technical Specification TS 38.141-1, Jan 2025.

Zahra Sepehri (Graduate Student Member, IEEE) received the Bachelor's degree in Electrical Engineering from Shiraz University in 2020. From 2018 to 2019, she worked as a teaching assistant at Shiraz University. Since 2022, she has been a graduate research assistant at École de technologie supérieure (ÉTS) in Montreal, Canada. She has been working as a teaching assistant while in graduate school. Her research focuses on the design of mm-wave devices, simulations, and measurements.

Gianluca Fabi (Member, IEEE) received the B.S. degree in Electronics Engineering from Marche Polytechnic University, Ancona, Italy, in 2015, the M.S. degree in Electronics Engineering from Politecnico di Torino, Turin, Italy, in 2017, and the Ph.D. degree from the Department of Information Engineering, Marche Polytechnic University, in 2021. He was a Post-Doctoral Researcher at the Department of Electrical and Computer Engineering, Cornell University, Ithaca, NY, USA. Since 2023, he has been with the Institute of Biophysics, Johannes Kepler University, Linz, Austria. Dr. Fabi's research interests include microwave circuits, devices, and characterization techniques.

Marco Farina (Senior Member, IEEE) received the M.S. and Ph.D. degrees in electronic engineering from Marche Polytechnic University, Ancona, Italy, in 1990 and 1995, respectively. He is currently a Professor of electromagnetics at the Università Politecnica delle Marche (Italy); Prof. Farina is in the Technical Committee of the IEEE MTT-Society "RF-Nanotechnology". He is the author of the electromagnetic modeling software EM3DS, used by a number of institutions and companies, including NASA, Intel, Mitsubishi, and also (optionally) embedded in Cadence "Microwave Office". Dr. Farina designed and realized a hybrid STM/Near Field Scanning Microwave Microscope. His research interests include electromagnetic modeling of passive and active components/structures, scanning probe microscopy, nanotechnology, and measurement techniques. He holds a patent for multi-modal calibration of VNA; the multi-modal calibration was awarded ITI-A and ITI-B contracts by ESA; he is also the inventor of the inverted Scanning Microwave Microscope (iSMM). He published papers in several international interdisciplinary conferences and journals. Dr. Farina is the co-recipient of the Best Conference Paper Award at the International Conference on Manipulation, Manufacturing and Measurement on the Nanoscale in 2014.

Richard Al Hadi (Senior Member, IEEE) received the engineering diploma from Caen's National Graduate School of Engineering in Electronics and Applied Physics and the Master degree from the University of Caen, France, in 2009. He received the Ph.D. degree, summa cum laude, from the University of Wuppertal, Germany, in 2014. In 2011, he was a Visiting Research Fellow at Korea University, Seoul, South Korea. He was with the University of California, Los Angeles (UCLA), CA, USA, in 2015 as a postdoctoral research fellow. He was with Alcatera Inc., Los Angeles, between 2017-2022. Since 2022, he is an Associate Professor at École de technologie supérieure (ÉTS), Montreal, QC, Canada. Dr. Al Hadi is a co-recipient of the 2012 Jan Van Vessem Award for the Outstanding European Paper at the IEEE International Solid-State Circuit Conference and the 2014 EuCAP best paper award.